2024 Tenth Indian Control Conference (ICC)
9 - 11 December, 2024
IISER Bhopal, India

System-Theoretic Insights into Battery Power Fade Prediction: A Probabilistic Framework

Sarnaduti Brahma[1] and Rishi Relan[1]

Abstract— **Accurate estimation of the power fade of a battery is crucial for its optimised usage and extended lifetime. Non-invasive techniques such as Electrochemical Impedance Spectroscopy (EIS) can be combined with machine learning to estimate power fade from externally measurable signals without damaging the battery. Traditional methods in the literature involve complete EIS curves obtained through separate sinusoidal excitations at various frequencies as features for training models, which is computationally intensive and time-consuming. This paper proposes a Gaussian Process Regression-based conformal prediction model for estimating a cell's power fade using EIS. The approach leverages system-theoretic concepts like multisine excitation, transfer function representation and subsequent pole-zero extraction. Multisine excitation allows for simultaneous excitation of relevant frequencies. At the same time, extracting only poles/zeros from EIS curves instead of using the entire EIS reduces the size of the training space, lowering computational resource requirements. Simulation results on a validated cell model demonstrate the accuracy of the proposed method across different temperatures in the presence of measurement noise.**

I. Introduction

Assessing a battery's state of health (SoH) during operation is critical to effectively managing its usage. The SoH measures a battery's present ability to store and deliver energy/power compared to that at the beginning of its life. It can be represented as either capacity fade or power fade (the reduced ability to provide power due to an increase in internal impedance). Over time, the SoH of a battery deteriorates due to structural degradation of the electrodes and/or unwanted side reactions [1]. Knowing the SoH allows the user to design an optimal control strategy, and make informed decisions for its future use, including when it should be decommissioned from the current operation and used for second-life applications.

The literature describes several non-invasive techniques for estimating the SoH that require only externally detectable signals such as temperature, voltage, or current to get an estimate of the SoH. These can be roughly categorized as data-driven and model-based techniques. Model-based approaches need an estimator such as the Kalman filter or its variations [2], to estimate the SoH in conjunction with a physics-based or an equivalent circuit model of the cell. But to do this, the model has to always reflect the physical cell's current state, with updated parameters that could be challenging to calibrate in real-time. Furthermore, physics-based models cannot be used in real-time due to their computational demands, which arise, e.g., from solving coupled partial differential equations.

Data-driven approaches, as opposed to model-based methods, make use of externally quantifiable signals such as voltage and current to estimate a cell's capacity or internal impedance. Differential thermal voltammetry [3], incremental capacity analysis [4], [5], and electrochemical impedance spectroscopy (EIS) [6] are a few examples. In the EIS approach, the cell is excited by sinusoidal current signals at multiple frequencies. The impedance of the cell as a function of excitation frequency is given by the ratio of the output voltage's frequency response to that of the input current. These impedance curves can be used to determine the age of the cell because, as a cell ages, its impedance increases.

Several SoH estimation techniques using EIS have recently been proposed in the literature that use EIS curves in conjunction with a machine learning-based regression model, such as neural networks [7], [8] or Gaussian process regression (GPR) [9], to provide estimates of battery SoH. Nevertheless, these techniques frequently employ complete EIS curves or specific segments as features to train a machine learning model, leading to a high dimensional training space. Alternatively, the EIS technique itself frequently involves successively stimulating the cell with sinusoids at various frequencies, which generates unwanted transients, and also takes a long time to generate the frequency response function (FRF). Lastly, when probabilistic regression techniques like GPR are applied, Bayesian credibility intervals—highly dependent on the prior distribution—are usually provided. These prediction intervals demonstrate a low coverage of the actual outputs if the real data does not align with the underlying assumptions about the probability distribution.

In this work, system-theoretic concepts of multisine excitation [10], transfer function representation, and subsequent pole-zero extraction are leveraged to develop a GPR-based data-driven model for the estimation of a cell's power fade. Additionally, conformal prediction intervals—as opposed to Bayesian intervals—are provided using the Jackknife+GP method [11]. Multiple frequencies are excited simultaneously using multisine excitation, which speeds up the computation of the impedance FRF. Pole-zero extraction provides a compressed representation of the EIS measurements that reduces space requirements and makes it suitable to be implemented in a battery management system. Simulating a validated cell model generates the required data for the model's development and testing. Test results show that high accuracy, with realistic prediction intervals, can be achieved.

[1]Sarnaduti Brahma and Rishi Relan are with Siemens Energy, Gurugram, India. {sarnaduti.brahma.ext, rishi.relan.ext}@siemens-energy.com

979-8-3315-1721-2/24/$31.00 ©2024 IEEE

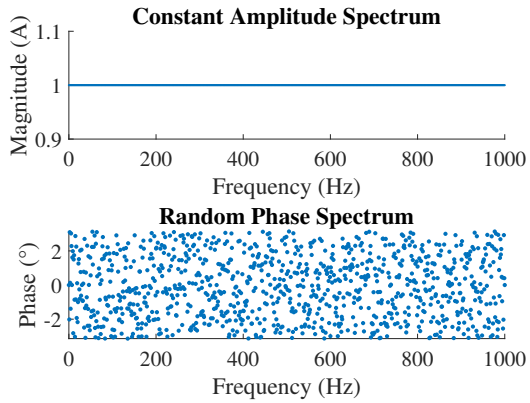


Fig. 1: A realisation of one-half of the Discrete Fourier Transform of one period of a random-phase multisine signal with a flat amplitude spectrum

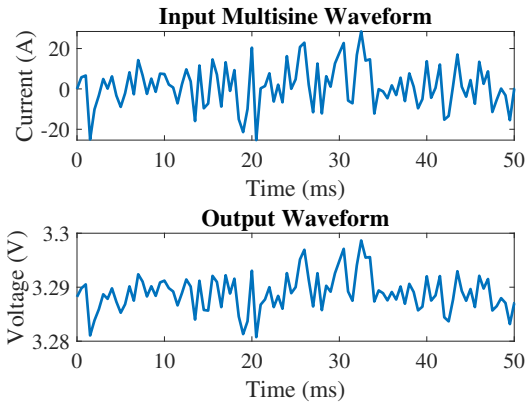


Fig. 2: Input multisine current waveform corresponding to Fig. 1 but scaled to 10 A RMS and the corresponding output voltage waveform zoomed to a 50 ms time window.

II. Data Generation and Preprocessing

A. Description of the simulation software package

Data were generated by simulating battery cells using a commercial software library composed of validated cell models in the Simulink® simulation environment. The commercial entity responsible for this library uses tests conducted on the physical cell at various SoH under pre-specified usage profiles, SoC, and temperatures to validate the models. Cells can be simulated using that program by setting the input voltage or current profile and a heat current input to set up the thermal environment. It is possible to specify the initial temperature as well as the initial SoC or open circuit voltage. In addition, the package lets one designate how much the cell is aged in terms of capacity or power. The internal parameters of the model are automatically calibrated to resemble the behavior of the real cell at that age, based on the ageing level chosen before the simulation.

B. Multisine Electrochemical Impedance Spectroscopy

In the conventional EIS approach, a cell is subjected to a series of small-amplitude sinusoidal current injections successively at various frequencies, and the voltage output produced when the cell is at rest is measured [12]. The ratio of the output's Fourier transform to the input's at those frequencies is then used to determine the FRF of this system. This offers a dynamic model that shows how the cell's impedance changes with frequency. The disadvantage of this approach is that it necessitates repeated simulations or tests for every frequency, which could be expensive or time-consuming in practical applications. The multisine excitation method, which involves exciting multiple frequencies simultaneously, eliminates transients that would appear with each change in frequency and is a faster way to identify a dynamic model of a system. In this paper, we apply this method from the field of system identification [10], [13].

A discrete-time multisine signal $i[k]$ is comprised of F harmonically related sinusoids of length N with possibly different amplitudes and phases, and is defined as follows:

$$i[k] = \sum_{l=1}^{F} A_l \cos\left(2\pi f_0 k l + \varphi_l\right),\ k = 0, 1, \ldots, N-1$$

where $A_l > 0$ and $\varphi_l \in (-\pi, \pi]$ are the amplitude and phase respectively of the l-th sinusoid, and $f_0 > 0$ is the fundamental frequency of the multisine [10].

For identifying a dynamic model for the cell, we consider a multisine current excitation signal $i[k]$ with a constant amplitude $A_l = A$ for all frequency components and a random phase that is uniformly distributed, i.e., $\varphi_l \sim \mathcal{U}(-\pi, \pi]$, resulting in a random-phase multisine with a flat amplitude spectrum. To generate this signal, first, a realization of its N-point Discrete Fourier Transform (DFT) $I[k]$ is designed in the frequency-domain (as shown in Fig. 1), with a resolution in the frequency axis equal to f_0, and then the time-domain signal $i[k]$ itself is obtained by taking its scaled Inverse DFT:

$$i[k] = \sum_{l=0}^{N-1} I[l] e^{j2\pi \frac{kl}{N} f_0}$$

The signal $i[k]$ is normalized by dividing it by its root-mean-square (RMS) value and multiplied by a number that the desired RMS value, i_{RMS}. We make the following assumption in this paper:

Assumption 1: The RMS value of the excitation signal, i_{RMS}, is much smaller than the 1C-rated current of the cell, while still large enough so that changes in the output voltage are higher than the resolution of the voltage sensor.

Remark 1: This assumption ensures that the nonlinearities in the cell are not sufficiently excited and that it can be approximated as a linear time-invariant (LTI) system during the identification process, while also ensuring that the sensors can pick up the voltage changes.

A longer input current signal is then formed by concatenating P periods of $i[k]$, and the cell is excited using this current at a sample time of $T_s = 1/f_s$, where $f_s = 2(N-1)f_0/N$, and its voltage output is recorded. An example input and output signal are shown in Fig. 2. The first period is discarded

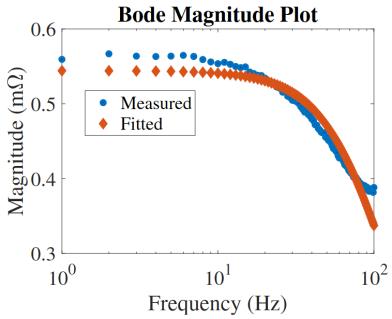


Fig. 3: Bode magnitude plot of measured and estimated Frequency Response Function

TABLE I: Simulation Parameters

Parameter	Range	Resolution
Power Fade	0 to 98%	2%
Initial Temperature	0°C to 40 °C	2°C
Initial SOC	5 to 95%	5%

to ensure transients have faded away. The outputs from each of the remaining periods are averaged to reduce the effect of noise. The scaled DFT of this averaged output $v[k]$,

$$V[k] = \frac{1}{N}\sum_{l=0}^{N-1} v[l]e^{-j2\pi\frac{kl}{N}f_0},$$

is then computed using a Fast Fourier Transform algorithm [14]. The ratio of one-half of the DFT of the output to that of the input is computed, which results in an FRF expressing the impedance $\mathcal{Z}$ of the cell as a function of frequency:

$$\mathcal{Z}(e^{j2\pi\frac{k}{N}f_0}) = \frac{V[k]}{I[k]} \tag{1}$$

Example curves of the magnitude and phase of an impedance measurement are shown in solid blue in Fig. 3.

C. Transfer function representation and pole-zero extraction

The transfer function $H(z)$ of a discrete-time LTI system with input $u[k] \in \mathbb{R}$ and output $y[k] \in \mathbb{R}$ that is described by the constant-coefficient difference equation:

$$\sum_{n=0}^{N} a_n y[k-n] = \sum_{m=0}^{M} b_m u[k-m],$$

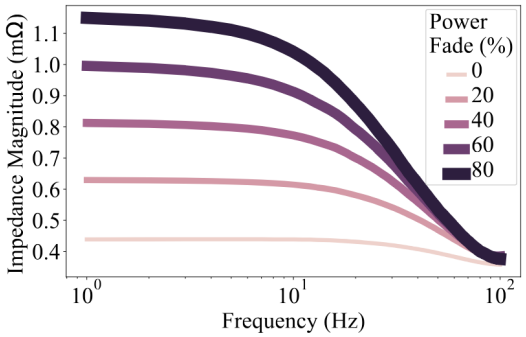
where $a_n, b_m \in \mathbb{R}$, is a rational function of $z \in \mathbb{C}$ given by:

$$H(z) = \frac{\sum_{m=0}^{M} b_m z^{-m}}{\sum_{n=0}^{N} a_n z^{-n}} \tag{2}$$

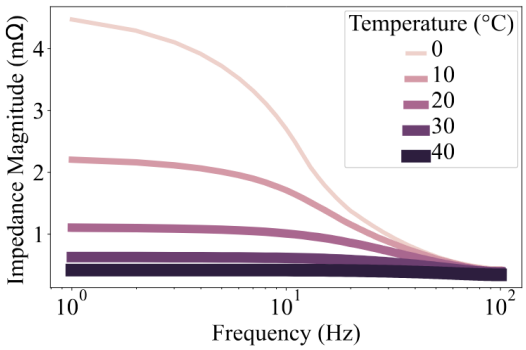
This function can be rewritten as:

$$H(z) = G\frac{\prod_{m=1}^{M}(z-z_m)}{\prod_{n=1}^{N}(z-p_n)} \tag{3}$$

where $z_m \in \mathbb{C}$, $m = 1, 2, \ldots, M$ are called the *zeros* and $p_n \in \mathbb{C}$, $n = 1, 2, \ldots, N$ the *poles* of the system, and $G \in \mathbb{R}$ is a constant gain factor. The zeros z_m can be extracted by finding the roots of the numerator of (2), and the poles p_m by those of the denominator [14].



(a) Varying power fade at 30°C and 50% initial SoC



(b) Varying temperature at 20% power fade and 50% initial SoC

Fig. 4: Impedance magnitude vs. frequency (smoothed using moving average filter) at varying power fade and temperature

Using the FRF obtained from measurements in (1), a transfer function $H(z)$ of suitable order (N, M) and values for the coefficients (a_n, b_m) can be *fitted* to the FRF (e.g., by using S-K iterations [15], as done by MATLAB®'s `tfest` command) such that the mean-squared error:

$$\sum_{k=0}^{N-1}\left|H(e^{j2\pi\frac{k}{N}f_0}) - \mathcal{Z}(e^{j2\pi\frac{k}{N}f_0})\right|^2$$

is minimized. This results in compressing the information contained in the impedance FRF measurements into a small number of zeros and poles.

D. Data analysis and feature selection

Using the commercial software package mentioned in Section II-A, multisine cell EIS measurements were carried out on a single 105 Ah capacity lithium iron phosphate (LFP) cell. The RMS value of the multisine current was taken to be $i_{\text{RMS}} = 10$ A. The current signal was designed to contain frequency components up to 100 Hz at a resolution of 10 Hz. Five periods of the multisine signal were used to excite the cell at various values of temperature, initial SoC, and power fade. The variable ranges are listed in Table I along with their resolution.

A few sample EIS impedance amplitude measurements are shown in Fig. 4. The amplitude of the impedance vs. frequency for changing power fade at 25°C and 50% initial SoC is displayed in Fig. 4a. The same is shown in

Fig. 4b for various initial cell temperatures at 20% power fade and 50% initial SoC. It is evident from Fig. 4 that temperature and power fade have a discernible impact on the EIS measurements. Furthermore, it was discovered that the EIS measurements for this cell were not significantly affected by the initial SoC. This might vary depending on the chemistry of the cells; in that case, other parameters must be considered while training the data-driven model.

After testing with different orders of transfer functions, it was found that a second-order transfer function, with two poles ($N = 2$) and a zero ($M = 1$), provided a reasonable fit to the FRF measurements to provide relevant features that correlate with power fade. Hence, a transfer function of the form:

$$H(z) = G\frac{z - z_1}{(z - p_1)(z - p_2)}$$

was fitted to these FRF measurements. In Fig. 3, the dashed red line illustrates an example of the Bode magnitude plot of the fitted transfer function. A strong correlation between temperature and one of the poles with power fade is seen in Fig. 5. In particular, it is seen that the pole moves toward the unit circle's edge as power fade increases, suggesting that the system dynamics slow down with ageing. To train a regression model to estimate the cell power fading, the two quantities—the temperature and the pole location—are thus utilized as features.

E. Generating noisy measurements

Sensors usually introduce measurement noise. Zero-mean additive white Gaussian noise was added to the output voltage to create additional datasets to recreate this situation and determine how the noise would affect the data-driven model. The noise standard deviation was adjusted to be between 0-1% of the mean voltage for this study.

III. Conformal Prediction using Gaussian Process Regression

A. Overview of Gaussian Process Regression

Consider that we have a training dataset $\mathcal{D}$ of n observations, $\mathcal{D} = \{(\mathbf{x}_i, y_i)|i = 1, \ldots, n\}$, where $\mathbf{x}_i \in \mathcal{X} \subseteq \mathbb{R}^m$ is a vector of m input feature values and $y_i \in \mathcal{Y} \subseteq \mathbb{R}$ the corresponding (scalar) output or target value of the i-th observation. The objective of regression is to produce a function $f : \mathcal{X} \to \mathcal{Y}$ using this dataset that can predict the output $\hat{y} = f(\mathbf{x})$ for any value of the input $\mathbf{x} \in \mathcal{X}$ as accurately as possible. There is a prediction error $y - \hat{y}$ since the prediction $\hat{y}$ does not match the actual observed output y at $\mathbf{x}$. Regression aims to minimise this error in some sense. Regarding the error, we assume the following:

Assumption 2: The prediction error ε is modelled by an independent and identically distributed (IID) zero-mean Gaussian distribution with variance σ_n^2, i.e., $\varepsilon = y - \hat{y} \sim \mathcal{N}(0, \sigma_n^2)$, where the notation $\mathbf{y} \sim \mathcal{N}(\boldsymbol{\mu}, \boldsymbol{\Sigma})$, in general, denotes that for an m-dimensional random vector $\mathbf{y}$ with mean $\boldsymbol{\mu}$ and covariance matrix $\boldsymbol{\Sigma}$, the probability density function (PDF) $p_{\mathbf{Y}}(\mathbf{y})$ is multivariate Gaussian, i.e.,

$$p_{\mathbf{Y}}(\mathbf{y}) = (2\pi)^{-\frac{m}{2}} \det(\boldsymbol{\Sigma})^{-\frac{1}{2}} \exp\left(-\frac{1}{2}(\mathbf{y} - \boldsymbol{\mu})^\top \boldsymbol{\Sigma}^{-1}(\mathbf{y} - \boldsymbol{\mu})\right)$$

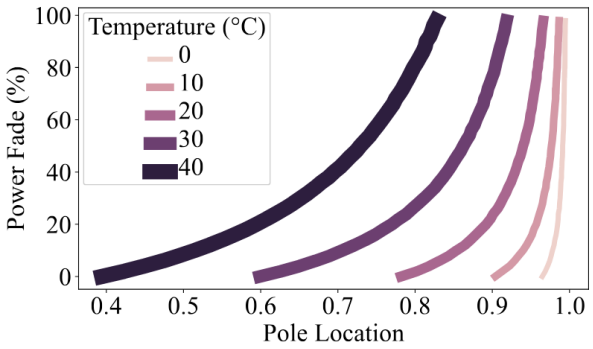


Fig. 5: Pole Location vs Power Fade

Remark 2: A zero mean ensures that there is no bias or offsets involved. This does not result in a loss of generality because one can add more elements to the input vectors $\mathbf{x}_i$ whose values are unity to incorporate a bias or offset. For a given sensor, a constant variance is reasonable as long as its physical characteristics remain unchanged.

In GPR, the output of the function f is assumed to be the output of an underlying Gaussian process. A Gaussian process is a collection of random variables (in this case $f(\mathbf{x}_i)$), any finite number of which have a joint Gaussian distribution [16]. It is completely specified by the mean function $m(\cdot)$ and the covariance function (also known as the *kernel*) $k(\cdot, \cdot)$, defined as follows:

$$m(\mathbf{x}_i) \triangleq \mathbb{E}[f(\mathbf{x}_i)]$$
$$k(\mathbf{x}_i, \mathbf{x}_j) \triangleq \mathbb{E}[\{f(\mathbf{x}_i) - m(\mathbf{x}_i)\}\{f(\mathbf{x}_j) - m(\mathbf{x}_j)\}]$$

such that $f(\mathbf{x}_i) \sim \mathcal{N}(m(\mathbf{x}_i), k(\mathbf{x}_i, \mathbf{x}_i))$, where $\mathbb{E}$ denotes the expectation operator. We make the following assumption:

Assumption 3: $m(\mathbf{x}_i) = \mathbb{E}[f(\mathbf{x}_i)] \equiv 0$

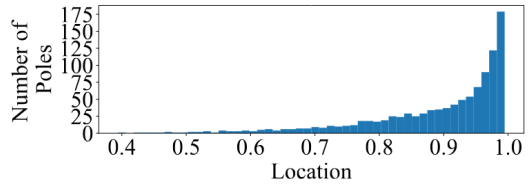
Remark 3: This presumption guarantees that the function output is free of bias and offset. Here, the same rationale as stated in Remark 2 holds.

With Assumption 3, the predictions $\hat{y}_i = f(\mathbf{x}_i) \sim \mathcal{N}(0, k(\mathbf{x}_i, \mathbf{x}_i))$. Further, let $\mathbf{X} = [\mathbf{x}_1^\top\ \mathbf{x}_2^\top\ \cdots\ \mathbf{x}_n^\top]^\top$ and $\hat{\mathbf{y}} = [\hat{y}_1\ \hat{y}_2\ \ldots\ \hat{y}_n]^\top$. Then, one can show that the PDF of the combined predicted output $\hat{\mathbf{y}}$ follows a multivariate Gaussian distribution: $\hat{\mathbf{y}} \sim \mathcal{N}(\mathbf{0}, K(\mathbf{X}, \mathbf{X}))$, where $K(\cdot, \cdot)$ produces an $mn \times mn$ covariance matrix from the entries of $\mathbf{X}$.

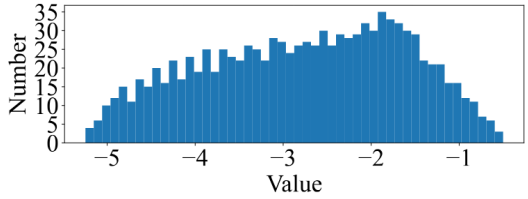
Consider an additional test dataset $\mathcal{D}_*$ of n_* observations, $\mathcal{D}_* = \{(\mathbf{x}_i^*, y_i^*)|i = 1, \ldots, n_*\}$, where $\mathbf{x}_i^* \in \mathbb{R}^m$ and $y_i^* \in \mathbb{R}$. Let $\mathbf{X}_* = [\mathbf{x}_1^{*\top}\ \mathbf{x}_2^{*\top}\ \cdots\ \mathbf{x}_n^{*\top}]^\top$ and $\hat{\mathbf{y}}_* = [\hat{y}_1^*\ \hat{y}_2^*\ \ldots\ \hat{y}_n^*]^\top$, where $\hat{y}_i^* \triangleq f(\mathbf{x}_i^*)$. Then, similar to above, $\hat{\mathbf{y}}_* \sim \mathcal{N}(\mathbf{0}, K(\mathbf{X}_*, \mathbf{X}_*))$. The joint conditional PDF of the predicted test outputs, conditioned on the training dataset and the test inputs, is ascertained by [16]:

$$\hat{\mathbf{y}}_*|\mathbf{X}_*, \mathbf{X}, \hat{\mathbf{y}} \sim \mathcal{N}\left(K(\mathbf{X}_*, \mathbf{X})[K(\mathbf{X}, \mathbf{X})^{-1} + \sigma_n^2\mathbf{I}]\hat{\mathbf{y}},\right.$$
$$\left. K(\mathbf{X}_*, \mathbf{X}_*) - K(\mathbf{X}_*, \mathbf{X})[K(\mathbf{X}, \mathbf{X}) + \sigma_n^2\mathbf{I}]^{-1}K(\mathbf{X}, \mathbf{X}_*)\right) \tag{4}$$

As seen above, GPR delivers a probability *distribution* of the prediction rather than a single *number* as deterministic



(a) Raw distribution of poles



(b) De-skewed distribution of transformed poles

Fig. 6: De-skewing the distribution of poles

regression techniques do. Furthermore, previous knowledge about the association between the input features can also be included in the model through a proper kernel definition.

B. Conformal prediction intervals

From the posterior PDF given by (4), a Bayesian $(1-\alpha)100\%$ credibility interval $C(\mathbf{x}_i^*) \subset \mathbb{R}$ can be obtained by evaluating the region where $\mathbb{P}(\hat{y}_i^* \in C(\mathbf{x}_i^*)|\mathbf{x}_i^*, \mathbf{X}, \hat{\mathbf{y}}) \geq 1-\alpha$, $0 < \alpha < 1$, for a test observation $(\mathbf{x}_i^*, \hat{y}_i^*)$. However, since for GPR the assumption is that the prior, and hence the posterior distribution, is Gaussian, a deviation of the underlying dataset from Gaussianity would result in inaccurate prediction intervals, such that the actual output may lie outside its prediction interval, leading to low "coverage".

This challenge can be resolved and realistic prediction intervals can be guaranteed regardless of the underlying distribution by using the framework of conformal predictions [11]. To show how unusual the test point is in relation to other points in the training dataset, the approach uses a nonconformity measure. Specifically, the credibility intervals for GPR are provided in our regression model by the Jackknife+GP conformal prediction estimator, which is specified in (26) of [11].

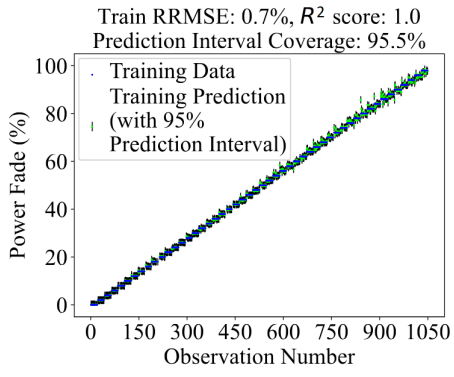
C. Formulation for power fade estimation

For the reasons outlined at the end of Section II-D, we have selected $\mathcal{D} = \{(\mathbf{x}_i, y_i)|i = 1, \ldots, n\}$ as the training dataset for our regression model, where the inputs $\mathbf{x}_i \in \mathbb{R}^2$ are the temperature in °C and the pole location, and the outputs $y_i \in [0, 100]$ are the corresponding power fade values in percentage.

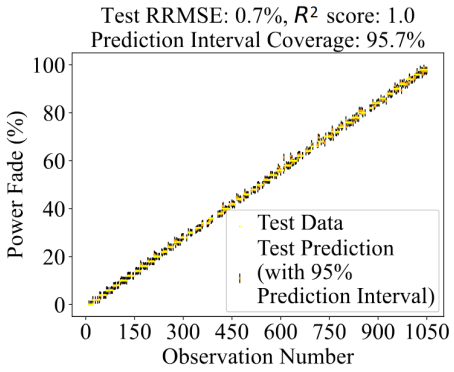
The kernel function $k(\cdot, \cdot)$ is chosen as the sum of the squared exponential kernel and a white noise kernel [16]:

$$k(\mathbf{x}_i, \mathbf{x}_j) = \text{cov}(f(\mathbf{x}_i), f(\mathbf{x}_j)) = \frac{\sigma_f^2}{2l^2}|\mathbf{x}_i - \mathbf{x}_j|^2 + \sigma_n^2 \delta_{ij}$$

where δ_{ij} is the Kronecker delta function whose output is unity if and only if $i = j$, and zero otherwise.



(a) Training Performance



(b) Test Performance

Fig. 7: Predictive performance of the GPR model with conformal prediction intervals

The regression model contains three hyperparameters that can be changed: the noise standard deviation σ_n, the characteristic length scale l, and the signal standard deviation σ_f. For accurate predictions, these hyperparameters must be tuned during training. For example, this can be done by employing a numerical optimization technique such as the limited-memory Broyden–Fletcher–Goldfarb–Shanno [17] to maximize the log-marginal-likelihood.

D. Preprocessing the data and performing GPR

It was noted that the distribution of one of the input features, the pole location, was strongly skewed to the left, before training the GPR model on the data produced in Section II-B (Fig. 6a). Therefore, a transformation $p' = \ln(1-p)$ was applied to the poles p to increase the model's accuracy. This produced a more symmetrical distribution for p' (Fig. 6b). The minimum and maximum values of each feature were then used to normalize the data between 0 and 1 to guarantee a consistent scale across features and enhance prediction accuracy. Using a random selection process, 80% of the dataset was separated into a training set, with the remaining 20% kept for testing. Using the `scikit-learn` package [18], the GPR model was constructed and trained, with its hyperparameters tuned, before being applied to the test dataset. The outputs were de-normalized. To achieve realistic estimates, the predicted output, power fade, was

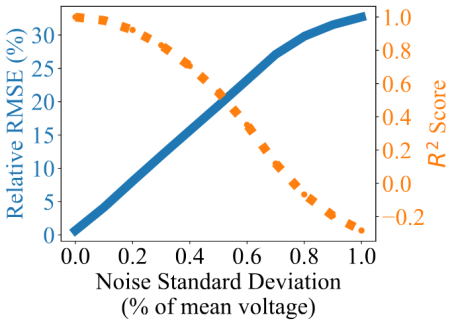


Fig. 8: GPR performance on noisy data

clipped to zero or 100% if it was projected to be less than zero or greater than 100%. The MAPIE package was used to generate the conformal predictions, which were clipped in the same way [19].

IV. Results and Discussion

A. Without noise

The GPR model's output in the absence of noise is displayed in Fig. 7. The power fade for each training data point (which consists of the modified pole location and temperature) is displayed in Fig. 7a. The actual power fade is indicated by the blue-coloured circle-shaped points, and the predicted power fade is indicated by the green-coloured plus-shaped points. The plus-shaped points have black error bars above them to represent the 95% prediction interval. As can be observed, most of the blue and green coloured points are nearly identical due to the closeness of the predicted and actual power fade. There is a 0.7% relative root mean squared error (RRMSE). Similar results are shown for the test dataset in Fig. 7b. Here, the predictions are shown in orange, and the actual power fade is represented in yellow.

B. With noise

The RRMSEs (solid blue curve) and R^2-scores (dotted orange curve) of the predictions on the noisy test dataset for a variety of noise variances are displayed in Fig. 8. This figure shows that the relative RMSE in the mean power fade prediction is less than 10% up to a noise standard deviation of 0.2% of the mean voltage (about 3.29 V in this case), while the R^2-score is greater than 0.9, suggesting that the method is robust to a small amount of noise and that the errors scale roughly linearly with the noise standard deviation.

V. Conclusion

To estimate a battery cell's power fade, a data-driven model utilizing GPR and poles obtained from multisine EIS measurements is developed in this work. A commercially validated cell model is used to generate the data. Even with added zero-mean Gaussian noise of variance of less than 0.2% of the mean voltage, the regression model's mean RRMSE of less than 1% suggests that the model is reasonably accurate. Future research will focus on creating comparable data-driven models to estimate ageing for dynamic applications utilizing additional non-invasive techniques such as differential thermal voltammetry.

References

[1] Y. Li, K. Liu, A. M. Foley, A. Zülke, M. Berecibar, E. Nanini-Maury, J. Van Mierlo, and H. E. Hoster, "Data-driven health estimation and lifetime prediction of lithium-ion batteries: A review," *Renewable and Sustainable Energy Reviews*, vol. 113, p. 109254, Oct. 2019.

[2] D. Andre, C. Appel, T. Soczka-Guth, and D. U. Sauer, "Advanced mathematical methods of SOC and SOH estimation for lithium-ion batteries," *Journal of Power Sources*, vol. 224, pp. 20–27, Feb. 2013.

[3] Z. Wang, C. Yuan, and X. Li, "Lithium Battery State-of-Health Estimation via Differential Thermal Voltammetry With Gaussian Process Regression," *IEEE Transactions on Transportation Electrification*, vol. 7, no. 1, pp. 16–25, Mar. 2021.

[4] D. Anseán, V. M. García, M. González, C. Blanco-Viejo, J. C. Viera, Y. F. Pulido, and L. Sánchez, "Lithium-Ion Battery Degradation Indicators Via Incremental Capacity Analysis," *IEEE Transactions on Industry Applications*, vol. 55, no. 3, pp. 2992–3002, May 2019.

[5] S. Brahma and R. Relan, "Online conformal prediction of battery capacity ageing from partial charging/discharging profiles," in *2024 23rd IEEE National Power Systems Conference (NPSC)*, 2024.

[6] P. Iurilli, C. Brivio, and V. Wood, "On the use of electrochemical impedance spectroscopy to characterize and model the aging phenomena of lithium-ion batteries: A critical review," *Journal of Power Sources*, vol. 505, p. 229860, 2021.

[7] C. Chang, S. Wang, J. Jiang, Y. Gao, Y. Jiang, and L. Liao, "Lithium-Ion Battery State of Health Estimation Based on Electrochemical Impedance Spectroscopy and Cuckoo Search Algorithm Optimized Elman Neural Network," *Journal of Electrochemical Energy Conversion and Storage*, vol. 19, no. 3, p. 030912, 04 2022.

[8] A. Eddahech, O. Briat, N. Bertrand, J.-Y. Delétage, and J.-M. Vinassa, "Behavior and state-of-health monitoring of li-ion batteries using impedance spectroscopy and recurrent neural networks," *International Journal of Electrical Power & Energy Systems*, vol. 42, no. 1, pp. 487–494, 2012.

[9] Y. Zhang, Q. Tang, Y. Zhang, J. Wang, U. Stimming, and A. A. Lee, "Identifying degradation patterns of lithium ion batteries from impedance spectroscopy using machine learning," *Nature Communications*, vol. 11, no. 1, p. 1706, Apr. 2020.

[10] R. Pintelon and J. Schoukens, *System identification: a frequency domain approach*. John Wiley & Sons, 2012.

[11] E. Jaber, V. Blot, N. Brunel, V. Chabridon, E. Remy, B. Iooss, D. Lucor, M. Mougeot, and A. Leite, "Conformal Approach To Gaussian Process Surrogate Evaluation With Coverage Guarantees," Jan. 2024, arXiv:2401.07733 [cs, stat].

[12] K. M. Kristensen, "Incremental Capacity Analysis (ICA) as a diagnostic tool for the State of Health (SoH) estimation of second Life Batteries," Master's thesis, Department of Energy Technology at Aalborg University (AAU), Aalborg, Dec. 2020.

[13] R. Relan, Y. Firouz, J.-M. Timmermans, and J. Schoukens, "Data-driven nonlinear identification of li-ion battery based on a frequency domain nonparametric analysis," *IEEE Transactions on Control Systems Technology*, vol. 25, no. 5, pp. 1825–1832, 2017.

[14] J. G. Proakis and D. G. Manolakis, *Digital signal processing (3rd ed.): principles, algorithms, and applications*. USA: Prentice-Hall, Inc., 1996.

[15] Z. Drmač, S. Gugercin, and C. Beattie, "Quadrature-based vector fitting for discretized $\mathcal{H}_2$ approximation," *SIAM Journal on Scientific Computing*, vol. 37, no. 2, pp. A625–A652, 2015.

[16] C. E. Rasmussen and C. K. I. Williams, *Gaussian Processes for Machine Learning*, 3rd ed., ser. Adaptive Computation and Machine Learning. Cambridge, Mass.: MIT Press, 2008.

[17] D. C. Liu and J. Nocedal, "On the limited memory BFGS method for large scale optimization," *Mathematical Programming*, vol. 45, no. 1, pp. 503–528, Aug. 1989.

[18] F. Pedregosa, G. Varoquaux, A. Gramfort, V. Michel, B. Thirion, O. Grisel, M. Blondel, P. Prettenhofer, R. Weiss, V. Dubourg, J. Vanderplas, A. Passos, D. Cournapeau, M. Brucher, M. Perrot, and E. Duchesnay, "Scikit-learn: Machine learning in Python," *Journal of Machine Learning Research*, vol. 12, pp. 2825–2830, 2011.

[19] V. Taquet, V. Blot, T. Morzadec, L. Lacombe, and N. Brunel, "MAPIE: an open-source library for distribution-free uncertainty quantification," Jul. 2022, arXiv:2207.12274 [cs, stat].